


RESEARCH ARTICLE

# Optical positioning technology of an assisted puncture robot based on binocular vision

Guanwu Jiang<sup>1</sup>  | Minzhou Luo<sup>2</sup> | Keqiang Bai<sup>1</sup>

<sup>1</sup>School of Information Engineering, Southwest University of Science and Technology, Mianyang, China

<sup>2</sup>Key Laboratory of Special Robot Technology of Jiangsu Province, Hohai University, Changzhou, China

## Correspondence

Guanwu Jiang, School of Information Engineering, Southwest University of Science and Technology, Mianyang 621010, China.

Email: jgwu0816@mail.ustc.edu.cn

and

Keqiang Bai, School of Information Engineering, Southwest University of Science and Technology, Mianyang 621010, China.

Email: baisir@mail.ustc.edu.cn

## Funding information

Key Research and Development Plan of Jiangsu Province, Grant/Award Number: BE2017603; Applied basic research project of the Science and Technology Department in Sichuan Province, Grant/Award Number: 19YYJC1670

## Abstract

Percutaneous image-guided interventions are increasing in number in clinical practice because they are minimally invasive. Needle positioning placement is crucial and highly dependent on the physician's skills and experience, it is often the longest part of the intervention. Medical robotics and computer-assisted surgery are hotspots in the field of robotics and medicine, changing the essence of traditional surgery using a combination of robotic, image processing, and computer technologies. The present paper aimed to study the auxiliary puncture procedure using a robot based on optical positioning technology that can be used to mark points in puncturing operation. Binocular camera is used for image acquisition, and Zhang's calibration method is used to establish the binocular camera model. In addition, the circular markers are identified by the least square method detection circle, and the coordinate information of the markers in three-dimensional space is solved by using the visual depth information of binocular phases. This paper studies the verification of the three-dimensional bone model of the human body, which lays a foundation for the application of the assistant puncture robot.

## KEYWORDS

acquisition of feature points, binocular camera, depth calculation, least square method, localization of puncture robot, optical positioning

## 1 | INTRODUCTION

Percutaneous image-guided interventions are increasing in number in clinical practice because they are minimally invasive.<sup>1</sup> Percutaneous puncture is a typical minimally invasive surgical procedure, which is guided by traditional medical images and operated by surgeons. The key to puncture surgery is to accurately obtain the insertion point on the skin and the focus in the body, and then determine the puncture path. With the development of computer, image processing, and robot technology, robot-assisted surgery has become a new research direction of puncture surgery. Medical CT image processing can realize the observation of internal organs and tissues, determine the position of internal focus and the position of the puncture route. The use of skin markers and robot-assisted puncture can achieve more

accurate positioning, which is of great significance in surgical operations.

Precise localization techniques for minimally invasive surgery can help surgeons quickly locate the puncture, especially during complex and difficult biopsy and ablation procedures. Infrared light-emitting diodes mounted on surgical instruments can be marked with the aid of a binocular camera and an infrared filter.<sup>2</sup> Luo et al. used binocular vision to extract the position and posture of the workpiece and proposed a background subtraction method to extract the feature points.<sup>3</sup> Dagnino et al. studied the application of the image-guided robotic system in the operation of fracture joint reduction, with the problem of fracture reduction being overcome by 3D image guidance from a double camera and a robot-assisted technique.<sup>4</sup> The application of image fusion and navigation in stratified mucin-producing intraepithelial

lesion tumors is applied and adopted an ActiViews optical tracking and positioning system.<sup>5</sup> The positioning of optical and electromagnetic tracking in lateral craniocerebral surgery is studied and verified that the optical tracking system was more accurate by Kral et al.<sup>6</sup> In order to realize the precise positioning of radiation patients and the accurate measurement of tumor location in the process of precise radiation therapy, a medical robot positioning system based on binocular vision is established.<sup>7</sup> A novel MRI-compatible puncture system was presented to ensure the safety of the puncture surgery by providing force feedback and image guidance and verifying a position deviation of  $\pm 1$  mm between the needle tip and the target point.<sup>8</sup> Hrdina and Návrát apply conformal geometric algebra (CGA) to the generalized binocular vision problem and reconstructs its 3D line from the image plane of the two cameras.<sup>9</sup> The positioning and servo method based on the optical tracker were studied to guide a percutaneous nephrostomy robot, which was used to simplify the registration process of the robot in the puncture operation and to complete the localization of the puncture with the help of ultrasonic guidance and optical assistance.<sup>10</sup> Placement accuracy of needle insertion into liver tissue was improved with the aid of a robot-assisted system, and the effect was significant with respect to an increase in controllability and stability.<sup>11</sup> Gao et al. studied the internal parameters of the binocular camera, the external rotation matrix, and the translation matrix through the application of a binocular vision positioning medical arm in precise radiosurgery.<sup>12</sup>

In this paper, medical puncture of skin markers in precise coordinate system is studied by using optical positioning method based on binocular vision measurement. In order to obtain the accurate positioning of the end position of the assistant puncture robot tool, the robot-guided fixture accurately locates the needle on the skin for accurate operation. Here, the use of binocular vision guided by skin markers to precisely locate the needle position to create a human spine model has proved to be more accurate than previous CT-guided and surgical procedures. The accuracy of puncture positioning is greatly improved and the operation time is significantly shortened, which meets the clinical requirements of robot-assisted positioning in minimally invasive surgery.

## 2 | SYSTEM DESIGN

### 2.1 | Framework and system composition

The puncture robotics system is highly demanded in medicine field due to its advantages such as achieving minimal invasiveness, accuracy, efficiency, and stability. The system is based on CT image processing and its three-dimensional (3D) reconstruction that guide a 6 degrees of freedom (DOF) robot toward precise positioning for minimal invasive surgery (MIS). The puncture robotic system is illustrated in Figure 1; its operation

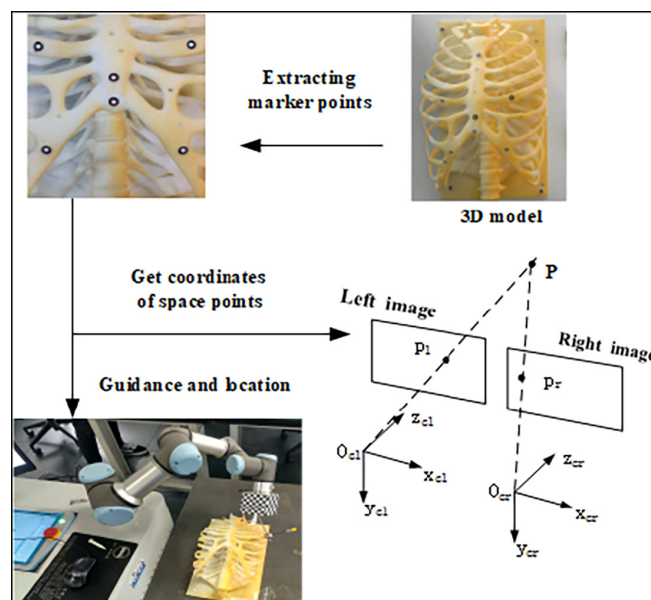


**FIGURE 1** Framework of optical tracking system [Color figure can be viewed at [wileyonlinelibrary.com](http://wileyonlinelibrary.com)]

is decided in the following steps. First, the patient is required to do CT scan. Then, a 3D model is reconstructed from the CT-scan image of the patient. Through the 3D model, doctor can observe and diagnose the disease. Second, the doctor determines the position of the puncture target point and the insertion point coordinates. The route must avoid the patient's bones, blood vessels, and other organs. The accurate puncture route determines the quality of the puncturing operation. Then, the target point and the insertion point coordinates are sent to the robot through the data processing computer.

The computer data processing system is the core of the entire auxiliary puncture robot, which completes the processing and 3D reconstruction of the binocular vision image and medical images, the registration of the coordinates, and the transfer of the motion instructions to the robot controller during the surgery. The framework of the proposed optical tracking system includes the main and auxiliary processes (as shown in Figure 1).

The auxiliary puncture robot and controller possess six DOF. Based on puncture surgery studies, the small UR3 robot with six DOF was selected as the collaboration robot from a universal robotic company. The robot itself weighs roughly 11 kg, with an effective load of approximately 3 kg. The working range is 500 mm, the 1-5 joint can be rotated by  $360^\circ$ , the sixth joint can be rotated indefinitely, and the repositioning accuracy reaches 0.1 mm. The robot controller is connected to the data processing computer through Ethernet communication. The robot can accept motion instructions from the computer and execute repositioning to the specified position.

The optical tracking system uses the binocular vision camera to collect the image, which completes the optical positioning of the patient's skin surface marker point, the

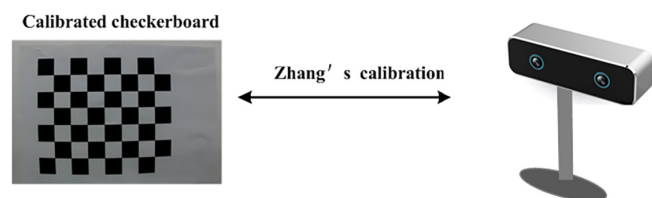


**FIGURE 2** Camera calibration [Color figure can be viewed at [wileyonlinelibrary.com](http://wileyonlinelibrary.com)]

coordinate system in the robot space, and the information collection of the position and posture of the robot's end. The auxiliary puncture process consists of binocular camera calibration, image acquisition, auxiliary puncture instrument positioning, patient skin marker point coordinate positioning, and transfer of instructions by the data processing computer to assist the puncture robot in executing the puncture localization with accurate position and posture.

The camera was calibrated using "Zhang's calibration," which refers to the camera calibration method involving a single plane checkerboard proposed by Professor Zhang Zhengyou in 1998.<sup>13</sup> This method lays between the traditional calibration and the self-calibration methods. Through the camera, the calibration checkerboard is photographed from different directions, and a sequence group of the left and right images is obtained. The defect of the high precision calibration object is overcome by the traditional calibration method, and the relationship moments between the mark points and the plane image points are obtained. Subsequently, the array, which is the internal parameters of the camera, is calculated. In the present study, the camera and a  $7 \times 8$  square black-and-white calibration checkerboard (as shown in Figure 2) were used; the size of the square was  $24 \times 24$  mm and the precision of the size error was 0.2 mm.

## 2.2 | Experimental setup

We developed a computer Graphical User Interface (GUI) visualization system for doctors based on the CT image. For simulating the system, we designed a 3D model typify the chest. The experimental setup is shown in Figure 3. The marks on the 3D model in black and white colors are for image processing purposes. Next, we take CT scan for the 3D model. We insert these images in our developed GUI system. The doctor can choose the insert point and target point through the GUI system. Then, we commanded the robot to position the end effector at the insertion point.

In this paper, the binocular camera is selected for image acquisition, extraction, and feature point matching, and accurate skin markers are provided in patients with needle coordinates, as shown in Figure 4. The binocular camera is calibrated by the needle position information on the calibration board, and the needle position is obtained by the calibration space coordinates of the markers on the skin. Position information of the calibration plate of the binocular camera is derived from the precise position of the end of the six-DOF manipulator.

## 2.3 | Robot tracking

During the operation, the robot moves the needle in the 3D space according to the computer. The puncture-guided instrument accurately positioned the tip of the needle on the patient's epidermis, and the surgeon performed the puncture. In the process of robot motion, the optical image acquisition and measurement space are transformed into the base coordinate space of the robot. In solving the inverse kinematics of the robot, the ideal position of each joint is obtained, and the motion of the robot is accurately controlled. At the same time, the position and posture of the robot are measured by

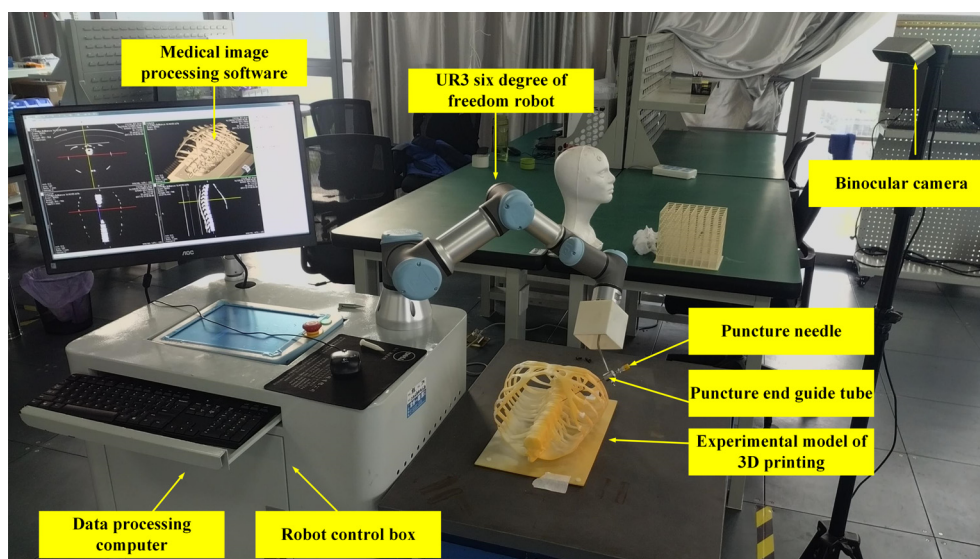


**FIGURE 3** Experimental setup, showing the GUI, 3D chest model and needle guide tube end-effector [Color figure can be viewed at [wileyonlinelibrary.com](http://wileyonlinelibrary.com)]

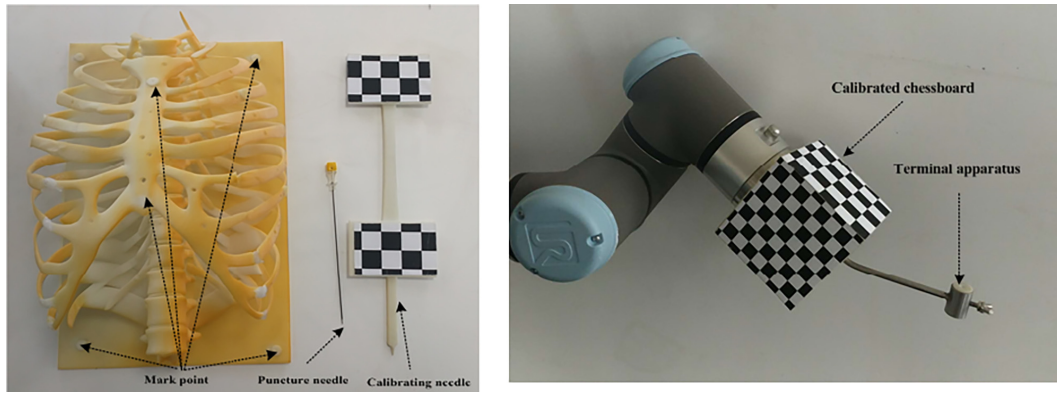


**FIGURE 4** Diagram of the 3D model mark points and demarcated needle and the end of the manipulator calibration plate [Color figure can be viewed at wileyonlinelibrary.com]

optical tracking and transmitted to the computer. The accurate trajectory tracking and positioning can be achieved by using a computer to correct the end position of the robot. Finally, after reaching the target point, the robot is locked on the operating platform, and the surgeon installs the surgical instruments at the end of the robot and performs the operation.

### 3 | MATERIALS AND METHODS

#### 3.1 | Model of vision sensor

The stereo imaging process projects 3D objects onto a 2D image plane using the world coordinate, camera coordinate, image pixel coordinate, and physical coordinate systems of the geometric transformation process. The object projection in the objective world is projected onto the 2D image pixel coordinate system using the 3D information, and the calibration information is combined to recover the established mathematical model.

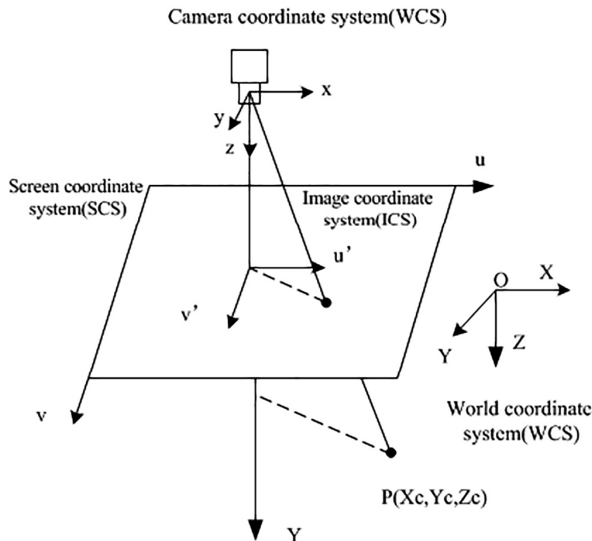


**FIGURE 5** Optical imaging coordinate system

The process of a commonly used camera pinhole imaging model is shown in Figure 5, and the spatial coordinates of the optical system are established. The camera coordinates, O-xyz, the image frame, O'-u'v', the screen frame, O'-u'v', the world coordinate system (WCS), O-xyz, and point P(Xc, Yc, Zc) is any point in the WCS.

The origins of the camera coordinate system are chosen as the center of the camera, and the z-axis coincides with the optical axis of the camera. The x and y axes coincide with the u' and v' axes of the image coordinate system. The transformation of the homogeneous coordinates of the space point P in the WCS  $(X_w, Y_w, Z_w, 1)^T$  with the homogeneous coordinates  $(x, y, z, 1)^T$  in the camera coordinate is shown as follows:

$$\begin{bmatrix} x_c \\ y_c \\ z_c \\ 1 \end{bmatrix} = \begin{bmatrix} {}^c_w\mathbf{R} & \mathbf{T} \\ 0 & 1 \end{bmatrix} \begin{bmatrix} X_w \\ Y_w \\ Z_w \\ 1 \end{bmatrix} \quad (1)$$

where  ${}^c_w\mathbf{R} = \begin{bmatrix} r_{11} & r_{12} & r_{13} \\ r_{21} & r_{22} & r_{23} \\ r_{31} & r_{32} & r_{33} \end{bmatrix}$  is the orthogonal rotation matrix and  $\mathbf{T} = [t_x, t_y, t_z]^T$  is the translational matrix.

The position of the space point P in the image can be approximated using a pinhole model, that is, the projection position of the point on the image is P' as the intersection of the line between the center O and point P in the image plane, where (u', v') are the coordinates of the P point in the image coordinate system,  $(x_c, y_c, z_c)$  are the coordinates of the P point in the camera coordinate system, and its homogeneous coordinate matrix is shown as follows:

$$z_c \begin{bmatrix} u' \\ v' \\ 1 \end{bmatrix} = \begin{bmatrix} f & 0 & 0 & 0 \\ 0 & f & 0 & 0 \\ 0 & 0 & 1 & 0 \end{bmatrix} \begin{bmatrix} x_c \\ y_c \\ z_c \\ 1 \end{bmatrix} \quad (2)$$



The pixel coordinate system and the image plane coordinate system comprise only the origin of coordinates, and their respective unit scales are not the same. The  $u$  and  $v$  axes are parallel to the  $u'$  and  $v'$  axes, and the coordinates of each pixel on the screen ( $u, v$ ) are the rows and columns of the pixels in the array, respectively. The coordinates of the intersection in the screen coordinate system are  $u_0$  and  $v_0$ . The actual physical dimensions of the unit pixels are  $d_x$  and  $d_y$ . According to the above relationships, the transformation relationships from the WCS to the screen coordinate system can be derived as follows:

$$\begin{aligned} z_c \begin{bmatrix} u \\ v \\ 1 \end{bmatrix} &= \begin{bmatrix} \frac{1}{dx} & 0 & u_0 \\ 0 & \frac{1}{dy} & v_0 \\ 0 & 0 & 1 \end{bmatrix} \begin{bmatrix} f & 0 & 0 & 0 \\ 0 & f & 0 & 0 \\ 0 & 0 & 1 & 0 \end{bmatrix} \begin{bmatrix} R & T \\ 0 & 1 \end{bmatrix} \begin{bmatrix} X_w \\ Y_w \\ Z_w \\ 1 \end{bmatrix} \\ &= \begin{bmatrix} a_x & 0 & u_0 \\ 0 & a_y & v_0 \\ 0 & 0 & 1 \end{bmatrix} [R|t] \begin{bmatrix} X_w \\ Y_w \\ Z_w \\ 1 \end{bmatrix} = MP_W \end{aligned} \quad (3)$$

where  $a_x = f/dx$  is the scale factor on the  $x$ -axis and  $a_y = f/dy$  is the scale factor on the  $y$ -axis.  $M$  is the camera's internal parameter matrix, determined by  $a_x$ ,  $a_y$ ,  $u_0$ , and  $v_0$ .  $R$  and  $T$  are the external parameters of the camera, which determine the orientation of the camera relative to the WCS. Camera calibration is the process of determining the internal and external parameters of the camera.

Considering the distortion caused by manufacturing errors, there are two main categories: radial distortion and tangential distortion. Since the tangential distortion is very small, only radial distortion is taken into account. The radial distortion can be approximately described as follows:

$$\begin{bmatrix} \delta_x \\ \delta_y \end{bmatrix} \approx \begin{bmatrix} x(r_1(x^2 + y^2) + r_2(x^2 + y^2)^2) \\ y(kr_1(x^2 + y^2) + r_2(x^2 + y^2)^2) \end{bmatrix} \quad (4)$$

where  $x$  and  $y$  are the coordinates of point  $P$  in the image coordinate system, and  $r_1$  and  $r_2$  are the radial distortion coefficients. Here, we only took the second items of the Taylor series expansion.

### 3.2 | Binocular stereo model

The depth information of the object can be obtained by using a binocular camera, and the 3D information about the object can be obtained by the parallax principle and the triangle method.<sup>14</sup> The 3D coordinate information of the camera midpoint can be obtained by the parameters of the binocular camera. The Binocular stereo imaging schematic is shown in Figure 6.

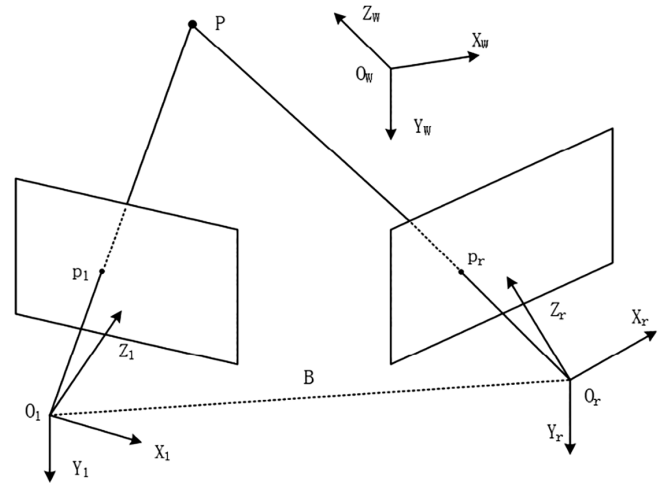


FIGURE 6 Binocular stereo imaging schematic

Binocular stereo vision requires that the internal and external parameters of the two cameras be calibrated as a single camera, then the relative position between the two cameras is calculated, and then the distance between the relative rotation of the two cameras and the center is calculated.  $O_w X_w Y_w Z_w$  is the WCS,  $O_l X_l Y_l Z_l$  is the left camera coordinate system,  $O_r X_r Y_r Z_r$  is the right camera coordinate system, and  $p_l$  and  $p_r$  are the image projection points of space point  $P$  on the plane of left camera and right camera, respectively.  $B$  is the distance between the center of light of the left camera and the right camera.

The rotation matrix from the right camera coordinate system to the left camera coordinate system is represented by  $R$ , and the translation vector from the right camera coordinate system to the left camera coordinate system is represented by  $t$ . Their relationship is shown as follows:

$$X_l = RX_r + t \quad (5)$$

where  $X_l$  and  $X_r$  represent the coordinates of 3D point  $P$  in left and right camera coordinates, respectively. If the rotation matrices  $R_l$  and  $R_r$  from world coordinates to left and right camera coordinates, as well as translation vectors  $t_l$  and  $t_r$ , are known, the following transformation relations exist:

$$\begin{cases} R = R_l R_r^{-1} \\ t = t_l - R_l R_r^{-1} t_r \end{cases} \quad (6)$$

Based on the above relations, various transformation relations and imaging processes of binocular stereo imaging are shown in Figure 7.

According to the pinhole imaging principle of the camera, it is set as a parallel binocular camera. The scale relation of imaging projection can be expressed as follows:

$$\begin{cases} \frac{f}{z_l} = \frac{u_l}{x_l} = \frac{v_l}{y_l} \\ \frac{f}{z_r} = \frac{u_r}{x_r} = \frac{v_r}{y_r} \end{cases} \quad (7)$$

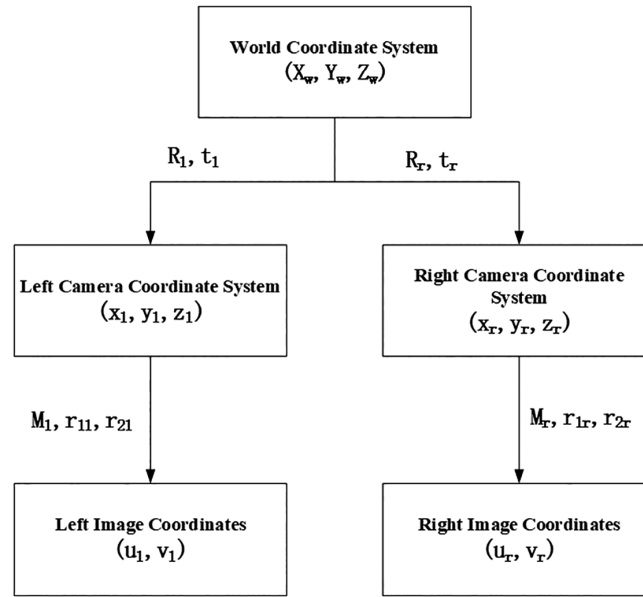


FIGURE 7 Binocular stereo imaging transform relation

When the WCS coincides with the left camera coordinate system, the relationship between the WCS and the camera coordinate system can be expressed as follows:

$$\begin{cases} X = x_l = x_r + B \\ Y = y_l = y_r \\ Z = z_l = z_r \end{cases} \quad (8)$$

Representation of horizontal parallax with  $D$  can be obtained in the same way as shown as follows:

$$D = x_l - x_r = \frac{Bf}{z} \quad (9)$$

$$\begin{cases} x_l = \frac{z_l u_l}{f} = \frac{z u_l}{f} \\ x_r = \frac{z_r u_r}{f} = \frac{z u_r}{f} \end{cases} \quad (10)$$

Points of the 3D coordinates in the camera coordinate system can be derived as follows:

$$\begin{cases} X = x_l = \frac{z u_l}{f} = \frac{u_l}{u_l - u_r} D \\ Y = y_l = \frac{z v_l}{f} = \frac{v_l}{u_l - u_r} D \\ Z = \frac{f}{\frac{u_l}{u_l - u_r}} \end{cases} \quad (11)$$

The WCS is coincident with the origin of the camera coordinate system, and the 3D coordinates of point  $P$  can be reconstructed by solving the coordinates of the pixels of the image captured by the left and right cameras.

### 3.3 | Least-squares edge fitting extraction method

The image of the target object with mark points is obtained by filtering, and the target in the image is found by the key

point extraction algorithm. The coordinates of the mark points in the binocular camera field of view are derived, as shown in Figure 7.

#### 3.3.1 | Edge extraction of circular marked points

In this study, circular marker points are selected and the coordinates of the center of the circle in binocular camera imaging are solved. In the 3D skeleton model, the extraction of circular marker points is transformed into the extraction of elliptic marker points. The ellipse detection process is shown as follows:

1. Input the region of interest (ROI) of the circular marker points and record the coordinates of the upper left corner of the ROI ( $x_0, y_0$ ).
2. Median filtering is applied to reduce the influence of noise on elliptic boundary without losing target information.
3. The image is binarized, and the pixel value of the background area is set to 0, and the pixel value of the circular marker area is set to 1.
4. To extract the edges of circular marker points, Canny operator is used to extract the edges of circular marker points.
5. By extracting the edge information and the upper left corner position coordinates ( $x_0, y_0$ ), the coordinate information of the circular marker points on the image can be obtained and pushed to its center coordinate information.

#### 3.3.2 | Round marker location by least-square edge fitting meter

After extracting the edges of circular marker points and obtaining the position information of all edge points, the least-square fitting method is used to restore the shape

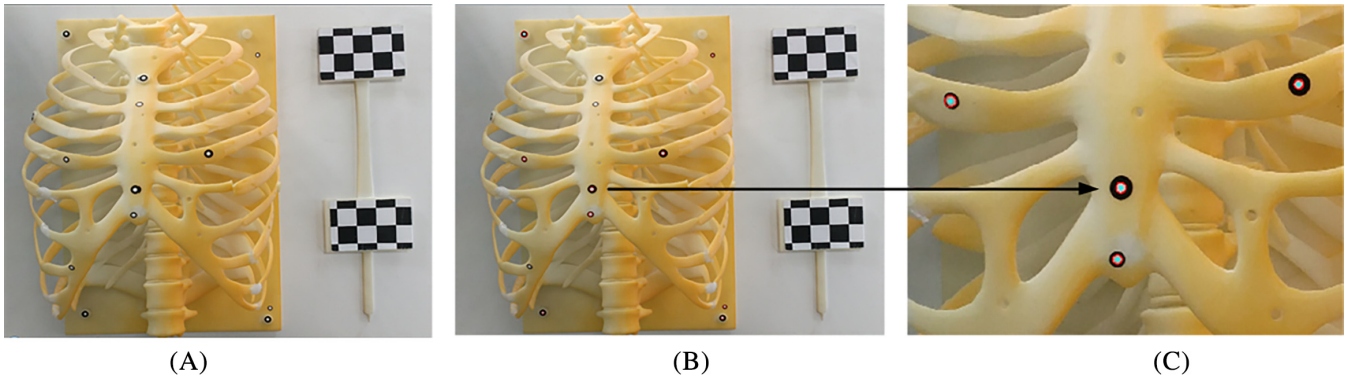


**FIGURE 8** Marker point acquisition: A, original plot; B, least square; and C, partial enlargement [Color figure can be viewed at [wileyonlinelibrary.com](http://wileyonlinelibrary.com)]

information of circular marker points.<sup>15</sup> The general expression of elliptic curve equation is as follows:

$$ax^2 + bxy + cy^2 + dx + ey + f = 0 \quad (12)$$

where,  $a, b, c, d, e$ , and  $f$  are coefficients of elliptic equation, and the formula is rewritten into matrix form:

$$\begin{bmatrix} x^2 & xy & y^2 & x & y & 1 \end{bmatrix} \begin{bmatrix} a \\ b \\ c \\ d \\ e \\ f+1 \end{bmatrix} = 1 \quad (13)$$

When the edge points  $(x_i, y_i)$  on multiple ellipses are known, they can be expressed in the following form:

$$\begin{bmatrix} x_1^2 & x_1 y_1 & y_1^2 & x_1 & y_1 & 1 \\ x_2^2 & x_2 y_2 & y_2^2 & x_2 & y_2 & 1 \\ \dots & \dots & \dots & \dots & \dots & \dots \\ x_i^2 & x_i y_i & y_i^2 & x_i & y_i & 1 \end{bmatrix} \begin{bmatrix} a \\ b \\ c \\ d \\ e \\ f+1 \end{bmatrix} = \begin{bmatrix} 1 \\ 1 \\ \dots \\ 1 \end{bmatrix} \quad (14)$$

$$\text{where } A = \begin{bmatrix} x_1^2 & x_1 y_1 & y_1^2 & x_1 & y_1 & 1 \\ x_2^2 & x_2 y_2 & y_2^2 & x_2 & y_2 & 1 \\ \dots & \dots & \dots & \dots & \dots & \dots \\ x_i^2 & x_i y_i & y_i^2 & x_i & y_i & 1 \end{bmatrix}, X = [a \ b \ c \ d \ e \ f+1]^T,$$

$B = [1 \ 1 \dots 1]^T$ , Formula (14) can be expressed as:

$$AX = B \quad (15)$$

According to the least squares, it can be obtained that

$$X = (A^T A)^{-1} B \quad (16)$$

Six coefficients of an ellipse can be obtained from  $X$ . When the characteristic coefficients of an ellipse are known, the outline of the ellipse can be fitted and the center of the ellipse  $(x_c, y_c)$  can be obtained, which can be expressed as:

$$\begin{cases} x_c = \frac{be - 2cd}{4ac - b^2} \\ y_c = \frac{bd - 2ae}{4ac - b^2} \end{cases} \quad (17)$$

### 3.3.3 | Marker point extraction

As shown in Figure 8A, a circular marker point coordinate is attached to the skeleton model, the marker point is selected as the inner diameter (3 mm) of the outer diameter (7 mm), and there are two checkerboard positioning plates on the marker needle to calculate the coordinate information of the pinpoint.

The images collected by binocular cameras contain a variety of noise, randomness, and irregularity, which can easily lead to image distortion and directly affect the accuracy of coordinate extraction of mark points. To smooth filtering and image processing, the commonly used filtering algorithms are mean filtering, median filtering, Gaussian filtering, and bilateral filtering. In this study, median filter algorithm is adopted, and  $3 \times 3$  filter window is selected according to the need. Median filtering algorithm effectively suppresses pulse interference and salt and pepper noise, effectively protecting image edges.

## 4 | RESULTS

### 4.1 | Parameter calibration of binocular vision system

In this paper, a binocular camera with a resolution of  $1920 \times 1080$  is selected. The binocular camera takes 20 groups of pictures at different positions and angles, as shown in Figure 8.

The intrinsic parameters and structural parameters of the binocular stereo vision system were calibrated using “Zhang’s calibration,” which refers to the camera calibration method involving a single plane checkerboard proposed by Professor Zhang Zhengyou in 1998.<sup>13</sup> The camera calibration toolbox in the Matlab software was used<sup>16</sup> for the calibration. As shown in Figure 9, the physical images of the calibration target were captured

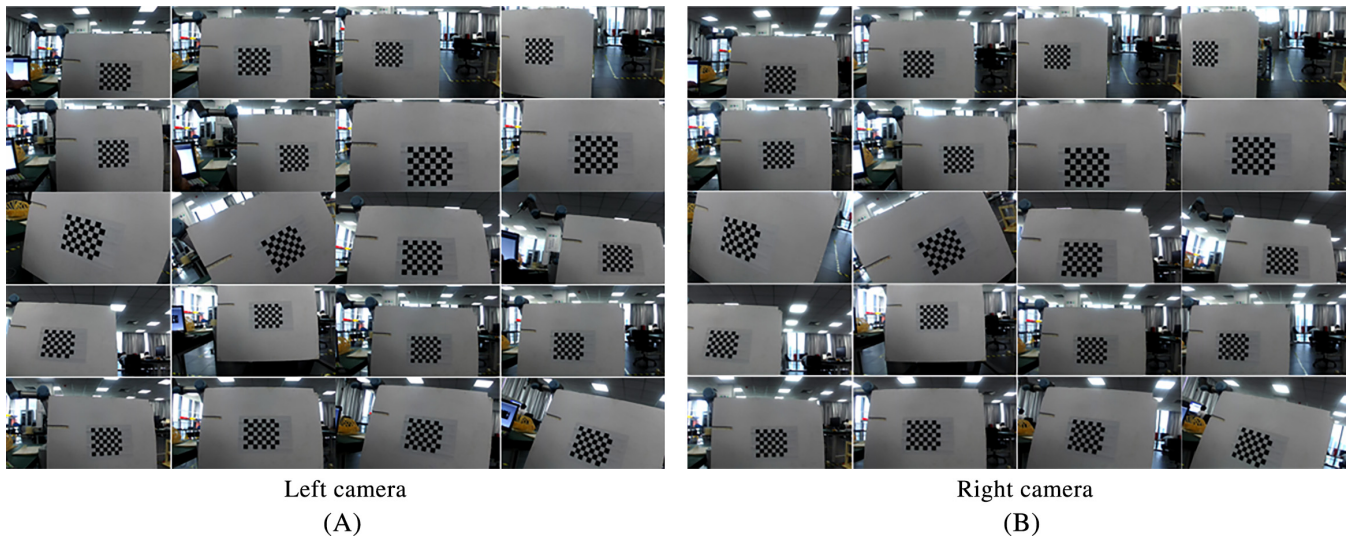


**FIGURE 9** Image contrast during the calibration process of the binocular camera [Color figure can be viewed at [wileyonlinelibrary.com](http://wileyonlinelibrary.com)]

by cameras. To improve the accuracy of the z-axis direction, 20 sets of calibration target images were collected at different angles and positions. The intrinsic parameters of the left and right camera were calculated according to the chessboard images of Figure 9A,B.

The structural parameters were calculated and combined with the chessboard images, which were used to describe the relative positioning relationship between the two cameras, where  $\mathbf{om}$  is the rotation vector of the right camera to the left camera, and  $\mathbf{T}$  is the translation vector of the right camera to the left camera.<sup>17</sup> Internal and external parameters of camera calibration of each camera are  $I_{\text{left}}$ ,  $I_{\text{right}}$  and  $E_{\text{left}}$ ,  $E_{\text{right}}$ , respectively.

$$I_{\text{left}} = \begin{bmatrix} 1394.236 & 0 & 985.89 \\ 0 & 1397.015 & 471.01 \\ 0 & 0 & 1 \end{bmatrix}$$

$$I_{\text{right}} = \begin{bmatrix} 1394.715 & 0 & 999.895 \\ 0 & 1397.391 & 516.335 \\ 0 & 0 & 1 \end{bmatrix}$$

$$\begin{bmatrix} 0.99990 & 0.00056 & -0.01218 & -119.9889 \\ -0.00038 & 0.99990 & 0.01416 & -0.0197 \\ 0.01219 & -0.01416 & 0.99980 & -0.4749 \\ 0 & 0 & 0 & 1 \end{bmatrix}$$

The left camera's optical center is used as the origin of the WCS. In this system,  $E_{\text{left}}$  is a fixed value as shown follows:

$$E_{\text{left}} = \begin{bmatrix} 1 & 0 & 0 \\ 0 & 1 & 0 \\ 0 & 0 & 1 \end{bmatrix}$$

The pixel coordinates of projection points are calculated according to the calibration parameters. Compared with the coordinates of the angle points directly extracted from the

image, the error distribution is shown in Figure 10. Figure 10A,B indicates that the projection error of the left and right cameras is within the range of 0.35 pixels.

After both the left and right cameras are calibrated, the parameters of the two cameras can be used for stereo calibration (as shown in Figure 11) and shows that the reprojection error of the image is near 0.167 pixels, and the calibration error is very small. Figure 10 is the 20 picture of the checkerboard marker fixed under the fixed binocular camera.

After binocular vision calibration, the parameters of the camera are obtained, and the parallax of the target points on the left and right views is calculated. It is necessary to match the pixels on the left and right views. Binocular correction will eliminate the distortion of the two images correspond strictly (as shown in Figure 12), so that the epipolar lines of the two images in the same horizontal line<sup>18</sup> and that the corresponding points on the left and right images of the same number through 1D search can be matched to the corresponding points.

The main reason for calculating the reprojection error is to extract the defect from the pixel coordinates of the target angle. When the depth of the field is small, the corner of the target is blurred, and there is a large extraction error, which will lead to the difference of camera parameters calibration.

## 4.2 | Space distance test

The circle-marked points were attached to the 3D model of the human skeleton, and the area containing the six mark points was selected as the location of the experiment. The ring marker point was selected as the outer diameter (7 mm) and the inner diameter (3 mm). The circle marker (red circle) was identified by the least squares method, and the blue point is the coordinate value of the center of the marker point, as shown in Figure 13. According to the above location verification method, the 100 cm range was measured



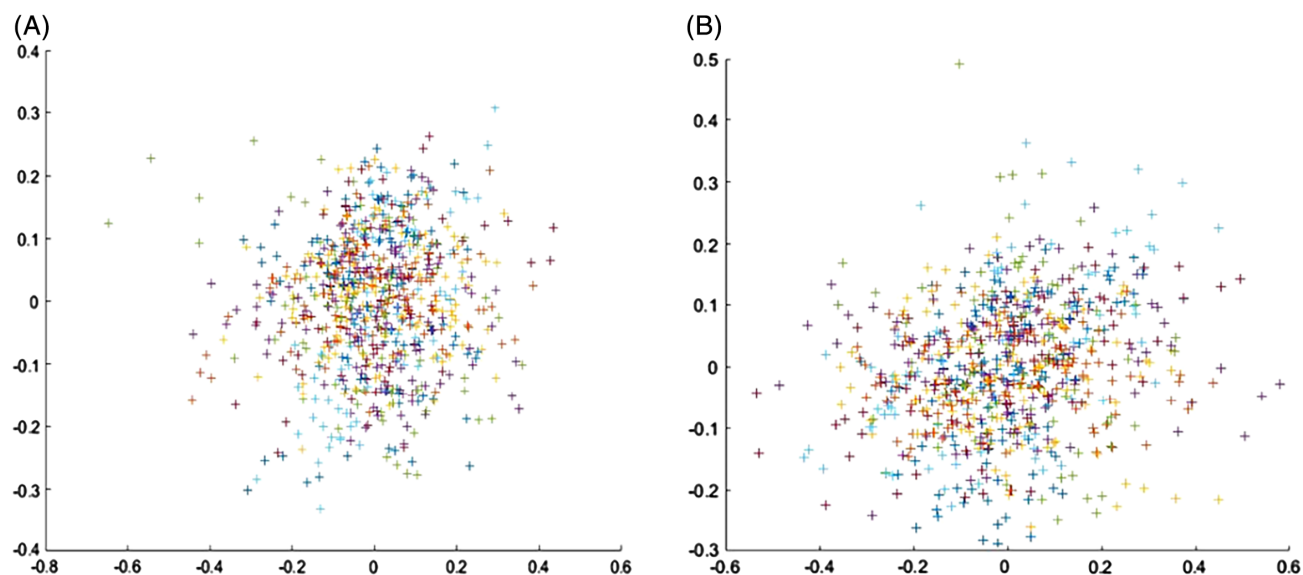


**FIGURE 10** Reprojection error of the checkerboard corner: A, reprojection error of the left camera; B, reprojection error of the right camera [Color figure can be viewed at [wileyonlinelibrary.com](http://wileyonlinelibrary.com)]

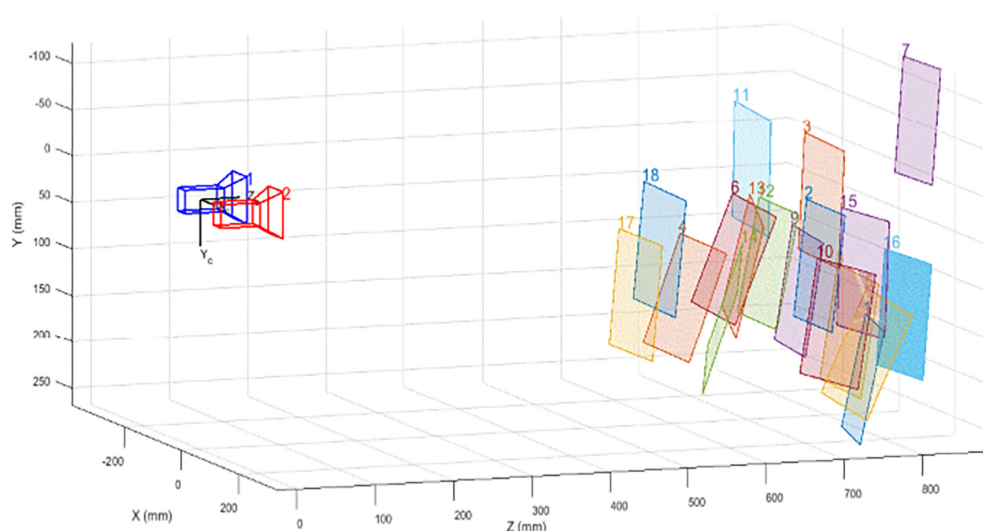


**FIGURE 11** The schematic diagram of binocular calibration results and camera fixed shooting [Color figure can be viewed at [wileyonlinelibrary.com](http://wileyonlinelibrary.com)]

and compared using a Vernier caliper and binocular vision image, as shown in Table 1.

In addition to feature point extraction and depth information, the 3D coordinate information in the target space is

obtained by matching algorithm, which lays a foundation for further research. Due to the nature of the camera hardware, there are some errors in the 3D position coordinates, but the X-axis and Y-axis errors are very small, in the range of

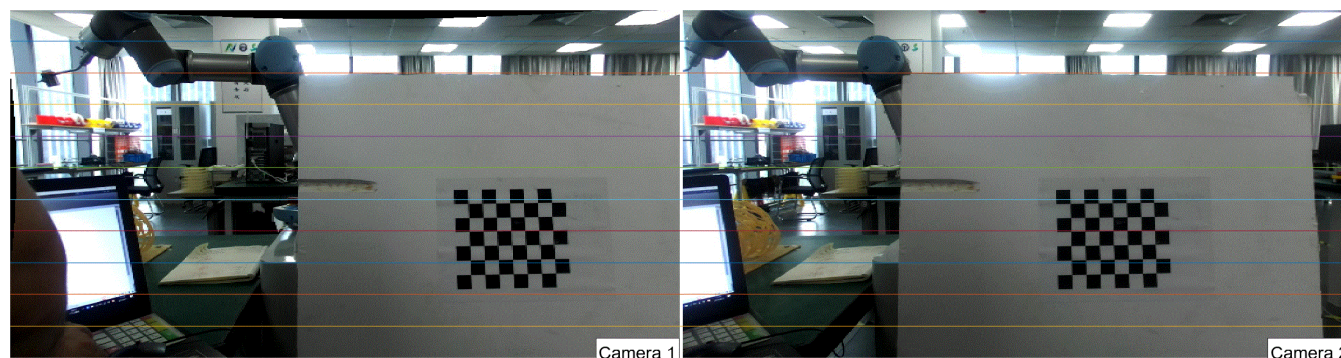


**FIGURE 12** Epipolar line plan of left and right images [Color figure can be viewed at [wileyonlinelibrary.com](http://wileyonlinelibrary.com)]

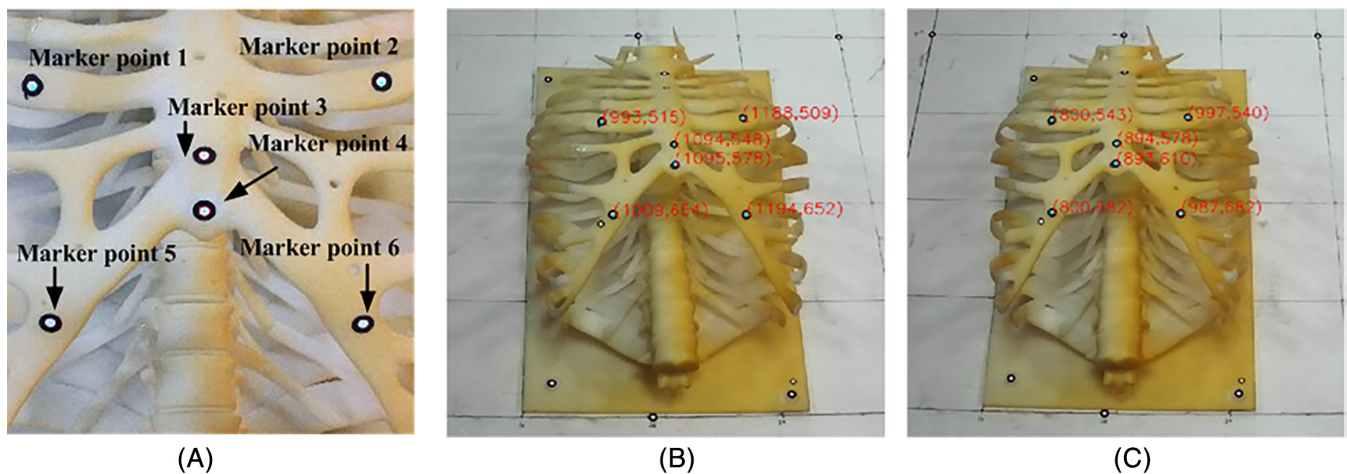


**FIGURE 13** Marker point recognition and coordinate acquisition graph: A, marker selection diagram; B, left camera marker point screen coordinates; and C, screen coordinates of the right image mark points [Color figure can be viewed at [wileyonlinelibrary.com](http://wileyonlinelibrary.com)]

**TABLE 1** Space distance test results for mark points

Marker point	$u_l$	$v_l$	$u_r$	$v_r$	$X_w$	$Y_w$	$Z_w$
1	993	515	800	542	660.7	10.2	1001.0
2	1188	509	998	539	780.0	7.1	999.3
3	1094	548	894	577	720.0	33.9	995.8
4	1195	578	893	610	721.3	57.9	995.6
5	1009	654	800	681	680.6	109.0	1002.4
6	1194	652	987	685	773.2	110.5	1000.8

2 mm. Z axis error is large, its range is 2–3 mm depth information. It is necessary to further study the accuracy of binocular camera algorithm.

## 5 | DISCUSSION

An optical tracking system based on the binocular camera is designed in this paper. According to the clinical requirement of precise location of human skin in medical puncture surgery, a method of precise location measurement for puncture robot based on binocular vision system is proposed. Using optical tracking system is difficult to match markers in traditional ways. This method can collect the skin markers quickly and accurately, and it can be verified by the skeleton model of the human body, to accurately locate the needle tip. In this paper, a new method of camera calibration based on a chessboard is studied, which is convenient for the identification of mark points. The coordinates of the center of a circular marker point can be identified, and the space coordinates of the marker point can be obtained in binocular coordinate system.

The system and related algorithms are meaningful explorations in the field of surgical navigation. The experimental results show that the 3D coordinates of skin markers and skin needles are obtained with the calibration of binocular camera. The fast calibration algorithm needs further study. The algorithm of pixel coordinate extraction and label

matching can also be optimized to improve the tracking accuracy of the system. Further optimization of real-time synchronization is needed to achieve higher system accuracy. At present, with more and more precise operational requirements, the accuracy and stability of the optical tracking system need to be improved. The deviation between the X and Y axes was 2 mm, the deviation from the Z axes was 2–3 mm, and the accuracy of the manual puncture position was significantly higher than that seen by previous surgeon-operated CT-guided methods. Besides, the operation time is short, which can meet the requirement of minimally invasive surgery. Specific clinical requirements for robot-assisted localization in sensitive surgery are mandatory; however, the study was carried out in the laboratory using a 3D skeleton model to achieve its function, and further research is needed to reach the clinical trial stage.

## ACKNOWLEDGMENT

This study was supported by funds from Applied basic research project of the Science and Technology Department in Sichuan Province (19YYJC1670) and the Key Research and Development Plan of Jiangsu Province (item number: BE2017603), and was verified by the Service Robot Laboratory of the Institute of Intelligent Manufacturing Technology of Jiangsu Industrial Technology Research Institute.

## ORCID

Guanwu Jiang  <https://orcid.org/0000-0002-1065-5268>

## REFERENCES

- Wood BJ, Ramkaransingh JR, Fojo T, et al. Percutaneous tumor ablation with radiofrequency. *Cancer*. 2002;94(2):443–451.
- Zhou Z, Wu B, Duan J, et al. Optical surgical instrument tracking system based on the principle of stereo vision. *J Biomed Opt*. 2017;22(6):1–14.
- Luo Z, Zhang K, Wang Z, et al. 3D pose estimation of large and complicated workpieces based on binocular stereo vision. *Appl Optics*. 2017;56(24):6822–6836.

4. Dagnino G, Georgilas I, Morad S, et al. Image guided surgical robotic system for percutaneous reduction of joint fractures. *Ann Biomed Eng*. 2017; 11(45):2648-2662.
5. Appelbaum L, Mahgerefteh SY, Sosna J, Goldberg SN. Image-guided fusion and navigation: applications in tumor ablation. *Tech Vasc Interv Radiol*. 2013;16(4):287-295.
6. Kral F, Puschban EJ, Riechelmann H, et al. Comparison of optical and electromagnetic tracking for navigated lateral skull base surgery. *Int J Med Robot*. 2013;9(2):247-352.
7. Feng D, Li S, Chang RU. Measurement method of medical robot positioning system based on binocular vision. *J Optoelectron Laser*. 2014;5(25):1027-1034.
8. Wang WD, Zhang P, Shi YK, Jiang QQ, Zou YJ. Design and compatibility evaluation of magnetic resonance imaging-guided needle insertion system. *J Med Imaging Health Infor*. 2015;5(8):1963-1967.
9. Hrdina J, Návrát A. Binocular computer vision based on conformal geometric algebra. *Adv Appl Clifford Algebr*. 2017;27:1945-1959.
10. Zhang D, Li Z, Chen K, et al. An optical tracker based robot registration and servoing method for ultrasound guided percutaneous renal access. *Biomed Eng Online*. 2013;12(47):1-16.
11. Wang W, Shi Y, Goldenberg A, et al. Experimental analysis of robot-assisted needle insertion into porcine liver. *Biomed Mater Eng*. 2015;26(S1): S375-S380.
12. Gao Y, Li J, Li J, et al. Modeling the convergence accommodation of stereo vision for binocular endoscopy. *Int J Med Robot*. 2017;1(14):1-13.
13. Zheng Z. A flexible new technique for camera calibration. *IEEE Trans Pattern Anal Mach Intell*. 2000;11(22):1330-1334.
14. Gai S, Da F, Dai X. A novel dual-camera calibration method for 3D optical measurement. *Opt Lasers Eng*. 2018;104:126-134.
15. Zhang M, Hu X, Zhao L, et al. Translation-aware semantic segmentation via conditional least-square generative adversarial networks. *J Appl Remote Sens*. 2017;11(4):1-31.
16. Camera Calibration Toolbox for Matlab, [http://www.vision.caltech.edu/bouguetj/calib\\_doc/](http://www.vision.caltech.edu/bouguetj/calib_doc/). Accessed October 14, 2015.
17. Lin C, Li Y, Xu G, et al. Optimizing ZNCC calculation in binocular stereo matching. *Signal Process Image Commun*. 2017;52:64-73.
18. Li W, Leung C, Hung Y. Matching of uncalibrated stereo images by elastic deformation. *Int J Imag Syst Technol*. 2004;14(5):198-205.

**How to cite this article:** Jiang G, Luo M, Bai K. Optical positioning technology of an assisted puncture robot based on binocular vision. *Int J Imaging Syst Technol*. 2019;29:180–190. <https://doi.org/10.1002/ima.22303>